Experimental Methods

1.1 Chemicals. Polyacrylonitrile (PAN), zinc acetate ($ZnAc_2$), $FeSO_4 \cdot 6H_2O$, $Zn(NO_3)_2 \cdot 6H_2O$, 2-methylimidazole (2-MeIM), H_2SO_4 solution (1.0 M), KOH solution (0.1 M), methanol, and *N*,*N*-dimethylformamide (DMF) were purchased from Wako Pure Chemical Industries. Nafion solution and Pt/C catalyst (20 wt.%) were purchased from Sigma-Aldrich.

1.2 Material Preparation

Synthesis of ZnAc₂/PAN (Zn/PAN) fibers. The synthesis of Zn/PAN fibers was established according to a previous literature.[1] Prior to electrospinning, a transparent solution with 10 wt.% $ZnAc_2$ was initially prepared by dissolving a certain weight of $ZnAc_2$ in 10 mL of hot DMF solvent (**Fig. S1a**). After that, a certain amount of PAN powder was added and dispersed without any precipitate remaining in the solution (**Fig. S1b**). Such a homogeneous mixture would guarantee the uniform distribution of Zn^{2+} in the final Zn/PAN fibers. For the electrospinning of Zn/PAN fibers, the solution with a flow rate of 10 mL h^{-1} per orifice was through a digital flow controller. The distance between the tip and collector was set at 30 cm. A gas pressure of 0.06 MPa and a voltage of 10 kV were applied. Finally, the prepared Zn/PAN fibers were dried at 70 °C overnight.

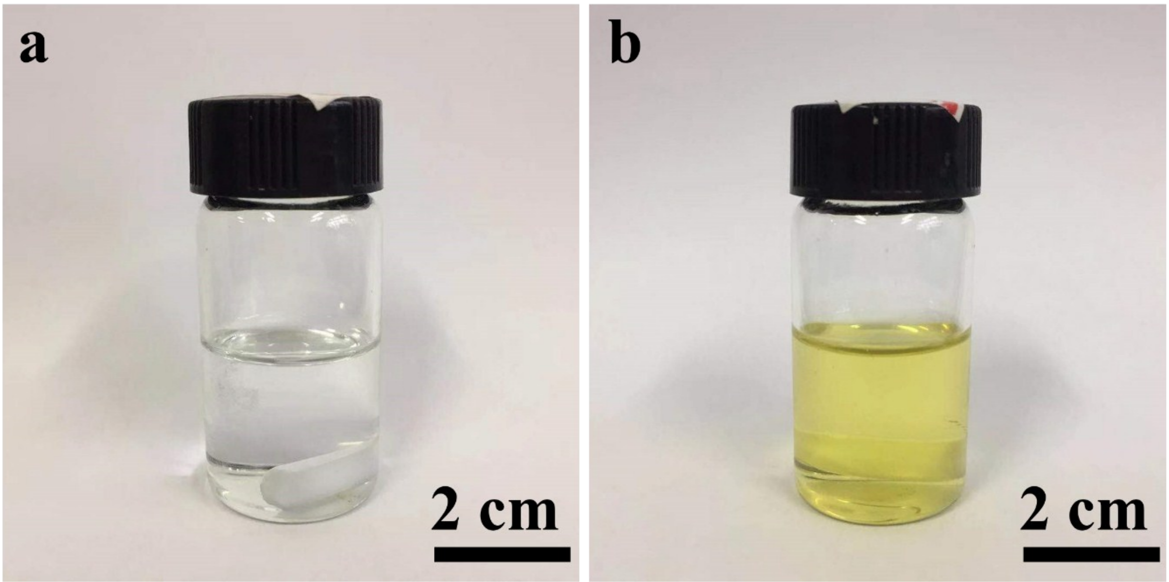

Fig. S1. Photographs of (a) $ZnAc_2$-containing DMF solution and (b) $ZnAc_2$/PAN-containing DMF solution.

Synthesis of PAN@ZIF' fibers. Typically, a certain amount of Zn/PAN fibers was immersed in a 2-MeIM methanolic solution (5 mM) for 30 min, leading to the decoration of Zn/PAN fibers with the first layer of ZIF. Then, the obtained ZIF-decorated PAN fibers were immersed in a methanolic solution of $FeSO_4/Zn(NO_3)_2$ (5 mM; molar ratio for $FeSO_4$ to $Zn(NO_3)_2$ is 5:95) for 30 min, covering Zn/PAN fibers with the first ZIF layer and the second ZIF' layer. By continuing the immersion of the Zn/PAN fibers in 2-MeIM methanolic solution and $FeSO_4/Zn(NO_3)_2$ methanolic solution alternately, Zn/PAN fibers covered with the third, fourth, and fifth layer of ZIF' were obtained. This process is referred to as layer-by-layer (LBL) growth technology.

Zn/PAN fibers covered with four ZIF’ layers were selected as the representative sample and abbreviated as PAN@ZIF’.

Synthesis of 3D-ZIF’ tubes. The PAN@ZIF’ fibers were dispersed in DMF at 60 °C to completely remove the Zn/PAN template to produce 3D-ZIF’ tubes.

Synthesis of 3D-FeNC tubes. The obtained 3D-ZIF’ tubes were obtained *via* a two-step heating, first at 350 °C and then at 900 °C under nitrogen atmosphere. Each stage was maintained for 2 h. The heating rate was set at 1 °C min^{-1} in the first stage (below 350 °C) and increased to 5 °C min^{-1} in the second stage (350 to 900 °C). 3D-FeNC tubes were finally obtained by treating the carbonized product in 1 M H_2SO_4 at 85 °C for 12 h, followed by a secondary heat-treatment at 900 °C for 2 h. The representative 3D-FeNC samples were prepared by using a methanolic solution containing $FeSO_4$ and $Zn(NO_3)_2$ (5 mM; molar ratio for $FeSO_4$ to $Zn(NO_3)_2$ is 5:95). In order to investigate the influence of Fe content on the ORR activity of 3D-FeNC, two other 3D-ZIF’ precursors were prepared by using methanolic solutions of $FeSO_4/Zn(NO_3)_2$ with different Fe^{2+} molar ratios of 2.5% and 7.5%. The corresponding materials are denoted as 3D-FeNC-2.5 and 3D-FeNC-7.5, respectively. The 3D-FeNC sample was also denoted as 3D-FeNC-5 for convenient comparison with 3D-FeNC-2.5 and 3D-FeNC-7.5.

Synthesis of ZIF’ tubes by using pure PAN fibers. Pure PAN fibers without Zn ions were also used as the template to grow ZIF’ layers *via* a similar LBL growth process for preparing PAN@ZIF’ fibers. The product was subsequently dispersed in DMF at 60 °C to completely remove the PAN cores for producing hollow ZIF’ tubes.

Synthesis of ZIF’ tubes by using a direct growth method. Zn/PAN fibers were immersed directly in $FeSO_4/Zn(NO_3)_2$/2-MeIM methanolic solution to grow ZIF’ layers. Next, the Zn/PAN cores were removed by DMF at 60 °C.

Synthesis of ZIF’ nanoparticles and the derived iron-nitrogen-doped carbon nanoparticles (p-FeNC). 25 mL of $FeSO_4/Zn(NO_3)_2$ methanolic solution (5 mM; molar ratio for $FeSO_4$ to $Zn(NO_3)_2$ is 5:95) was mixed with 25 mL of 2-MeIM methanolic solution (5 mM) under stirring. After 24 h, ZIF’ nanoparticles were collected by centrifugation, washed with methanol at least three times, and then dried at 60 ºC. p-FeNC was prepared by treating the ZIF’ nanoparticles with the same process as 3D-FeNC.

1.3 Materials characterization

The crystal structure and phase composition of the samples were characterized by powder X-ray diffraction (XRD) using an Ultima Rint 2000 X-ray diffractometer (RIGAKU, Japan) with Cu Kα radiation (40 kV, 40 mA, scan rate of 2° min^{-1}). The surface composition and elemental state of the samples were analyzed by X-ray photoelectron spectroscopy (XPS) using an Imaging Photoelectron Spectrometer (Axis Ultra, Kratos Analytical Ltd.) with a monochromatic Al Kα X-ray source. The porosity of the materials was characterized by N_2 adsorption-desorption measurements using a BELSORP-mini (BEL, Japan) at 77 K. Brunauer-Emmett-Teller (BET) method was used to estimate the specific surface areas (SSAs) of the samples by using the adsorption branch data in the relative pressure (P/P_0) range of 0.05-0.5. The morphology of the samples was checked by field-emission scanning electron microscope (FESEM, Hitachi SU8000, 5 kV). The field emission transmission electron microscope (TEM) images were taken with a JEOL JEM-2100. Fe K-edge X-ray absorption spectra (XAFS) were acquired at 1W1B beamline of the Beijing Synchrotron Radiation Facility (BSRF) in fluorescence mode at room temperature using a Si (111) double-crystal monochromator. The storage ring of BSRF was operated at 2.5 GeV with a maximum current of 250 mA in decay mode. The XAFS raw data were background-subtracted, normalized, and Fourier transformed by standard procedures using the ATHENA program. Least-squares curve fitting analysis of the extended XAFS $\chi(k)$ data was carried out using the ARTEMIS program. All fitting processes were performed in the R space with a k-weight of 3.

1.4 Oxygen reduction reaction (ORR) measurements

All ORR measurements were conducted on a CHI 842B electrochemical analyzer (CH Instrument, USA) in O_2/N_2 saturated 0.1 M KOH solution. The saturated calomel electrode (SCE) and Pt wire were used as reference electrode and counter electrode, respectively. The working electrode was prepared as follows: Firstly, 5 mg of the sample or Pt/C catalyst (20 wt.%) was dispersed in a mixture of isopropanol/water (1 mL, v/*v*=1:2) followed by the addition of 5.0 wt.% Nafion solution (0.05 mL) and subsequent sonication for approximately 30 min to form a homogenous catalyst ink. Next, the catalyst ink (5 μL) was drop-casted onto the surface of a glassy carbon (GC) electrode (Diameter: 4 mm, RRDE Pt Ring/GC Disk Electrode, cat. NO. 011162, ALS Co., Ltd.) with an areal loading of 0.2 mg cm^{-2}. Cyclic voltammetry (CV) measurements were performed in the potential range of 1.2 to 0.0 V with a scan rate of 50 mV s^{-1}. RRDE measurements were carried out by linear sweep voltammetry (LSV) with a scan rate of 10 mV s^{-1} in the potential range of 1.2 to 0.0 V, and various rotating speed (625 to 2500 rpm). The ring electrode potential was maintained at 1.2 V. The durability test was conducted by cycling the 3D-FeNC-5 or Pt/C catalyst from 0.6 to 1.0 V in O_2-saturated 0.1 M KOH solution with a scan rate of 50 mV s^{-1}. In addition, after the correction of double-layer capacitance, the current density was calculated based on the geometrical area (0.1256 cm^2) of the rotating disk electrode.

The ORR kinetics of the electrodes were analyzed by using the Koutecky–Levich (K-L) equation:

$$\frac{1}{j} = \frac{1}{B\omega^{1/2}} + \frac{1}{j_K} \quad \text{(S1)}$$

$$B = 0.62nFC_0{D_0}^{2/3}\upsilon^{-1/6} \quad \text{(S2)}$$

where j is the measured current density, ω is the electrode rotating rate, j_K is the kinetic current density, n is the number of transferred electrons, F is the Faraday constant (96485 C mol^{-1}), C_0 is the bulk concentration of O_2 (1.2×10^{-6} mol cm^{-3}), D_0 is the diffusion coefficient of O_2 (1.9×10^{-5} cm^2 s^{-1}), and υ is the kinematic viscosity of the electrolyte (0.01 cm^2 s^{-1}).

1.5 Capacitive deionization (CDI) measurements

The electrode for CDI was fabricated by depositing a mixture of the sample (mass loading: ~2.5 mg cm^{-2}) with Vulcan XC 72 and PVDF binder on graphite paper (thickness: 1 mm). The mass ratio of sample, Vulcan XC 72 and PVDF was 8:1:1. The mixture was pressed onto a graphite paper and dried under vacuum at 60 °C for 12 h. To fabricate the 3D-FeNC electrodes, 3D-FeNC samples with areal mass loading of ~2.5 mg cm^{-2} were directly used as CDI electrodes without any modifications.

Each CDI apparatus comprises a pair of identical electrodes (2×2 cm^2). Batch-mode desalination experiments were conducted in oxygenated saline water with a continuous recycling system, including a CDI apparatus, a peristaltic pump, a power source, and a tank. In each experiment, the real-time saline concentration, current, and pH variation were monitored and measured at the outlet of the CDI apparatus. The volume of the saline solution was fixed at 20 mL, the flow rate was maintained at 20 mL min^{-1}, and the operating voltage was 1.2 V.

The salt adsorption capacity (*SAC*, mg g^{-1}) and mean salt adsorption rate (*MSAR*, mg g^{-1} min^{-1}) at *t* min were calculated using the following equations:

$$SAC = (C_0 - C_t) \times V/m \tag{S3}$$

$$MSAR = SAC/t \tag{S4}$$

where C_0 and C_t represent the concentrations of NaCl at initial stage and *t* min, respectively (mg L^{-1}); *V* represents the volume of the NaCl solution (L), and *m* represents the total mass of the electrode material (g).

The charge density (Λ) and specific energy consumption (*E*, J mg^{-1}) were calculated according to the following equations:

$$\Lambda = SAC \times F \times m/M \Big/ \int_0^T i\,dt \tag{S5}$$

$$E = \int_0^T Ui\,dt \Big/ (m \times SAC) \tag{S6}$$

where *F* represents Faradic constant (96485 C mol^{-1}), *m* is the total mass of active materials (g), *M* is molecular weight of NaCl (58.44 g mol^{-1}), *T* is the electrosprtion time (s), and *U* is the operation voltage (V).

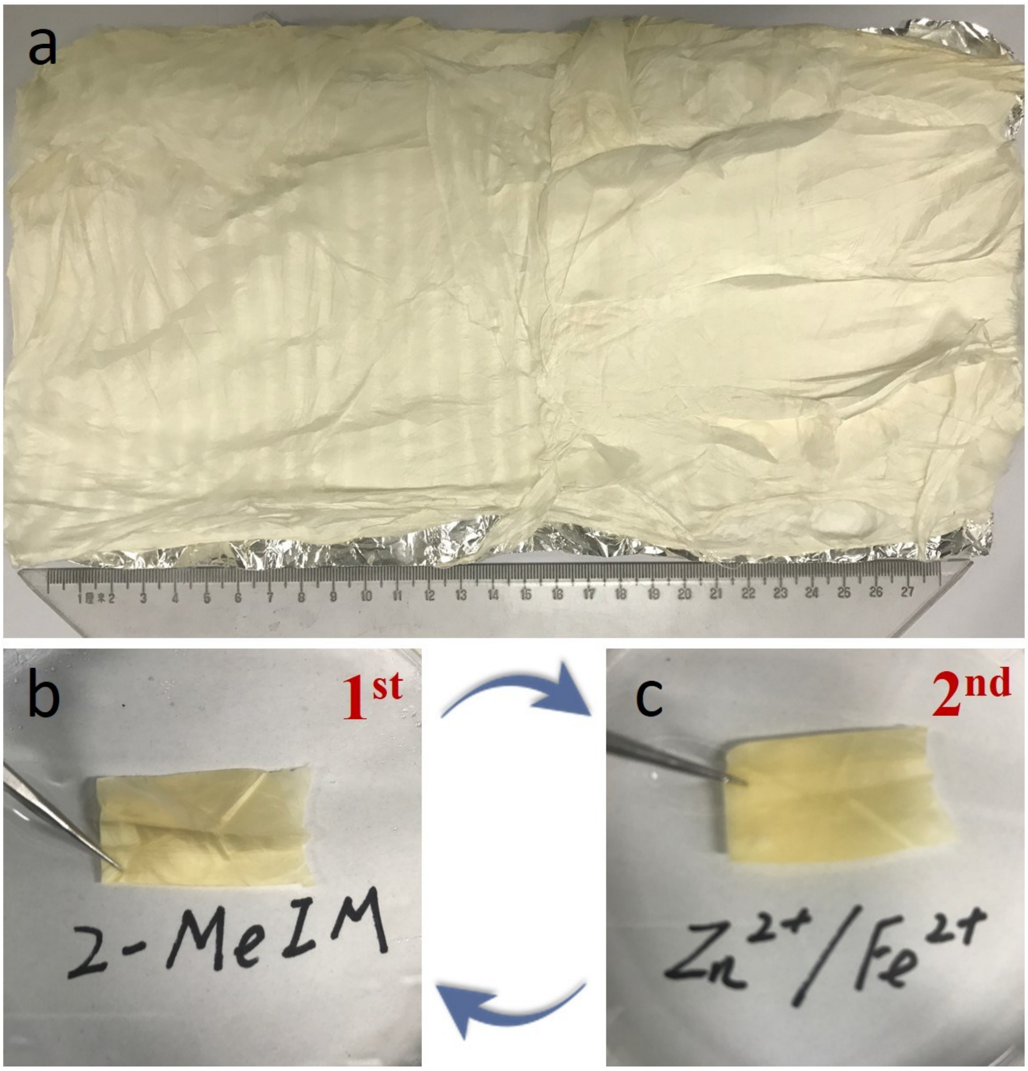

Fig. S2. Photographs of (a) Zn/PAN fibrous film and (b, c) LBL growth technology.

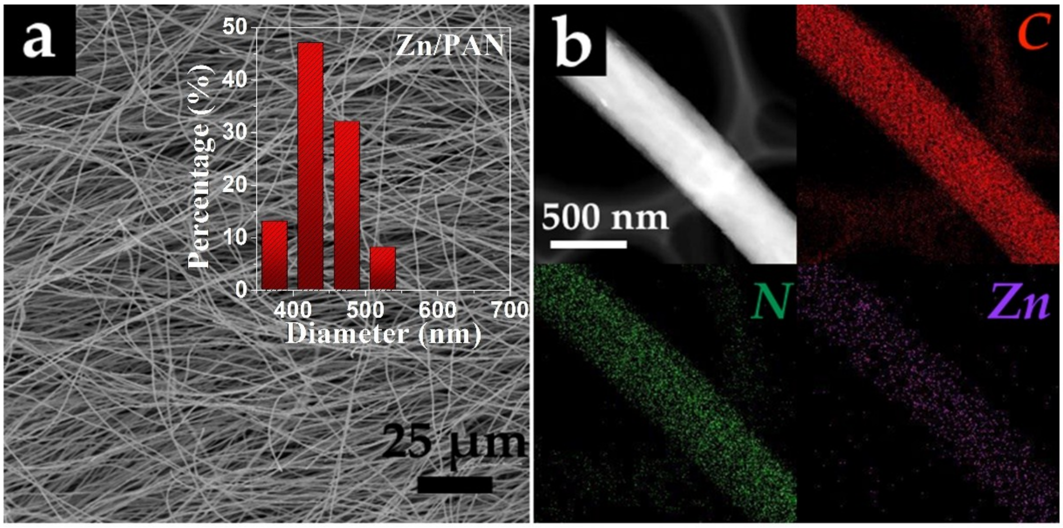

Fig. S3. (a) FESEM image of Zn/PAN fibers. Inset is the diameter distribution of Zn/PAN fibers calculated from the FESEM image; (b) High-angle annular dark-field scanning TEM (HAADE-TEM) and energy dispersive X-ray spectroscopy (EDX) elemental mapping images of a single Zn/PAN fiber.

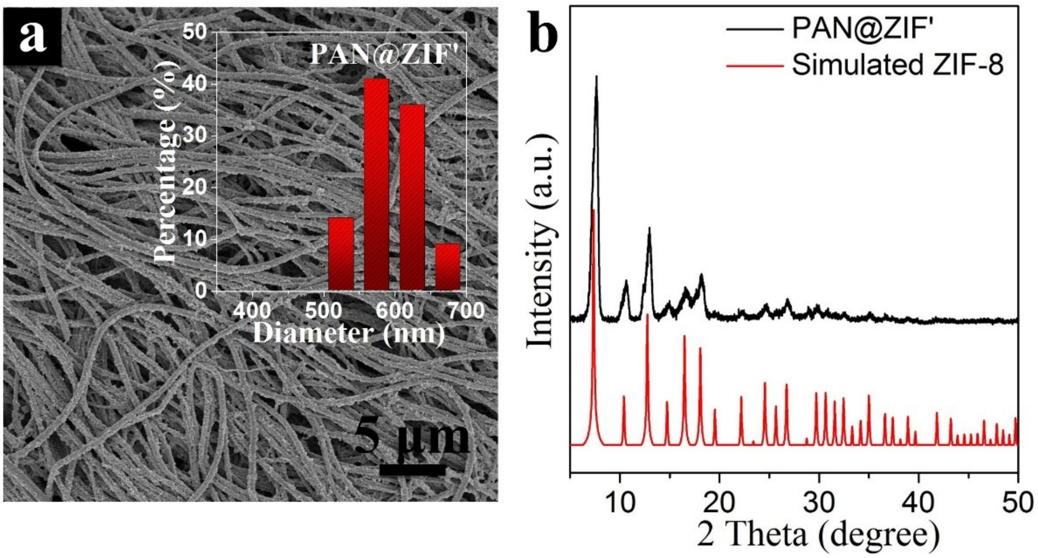

Fig. S4. (a) FESEM image of PAN@ZIF’ fibers. Inset is the diameter distribution of PAN@ZIF’ fibers calculated from the FESEM image; (b) XRD patterns of PAN@ZIF’ and simulated ZIF-8.

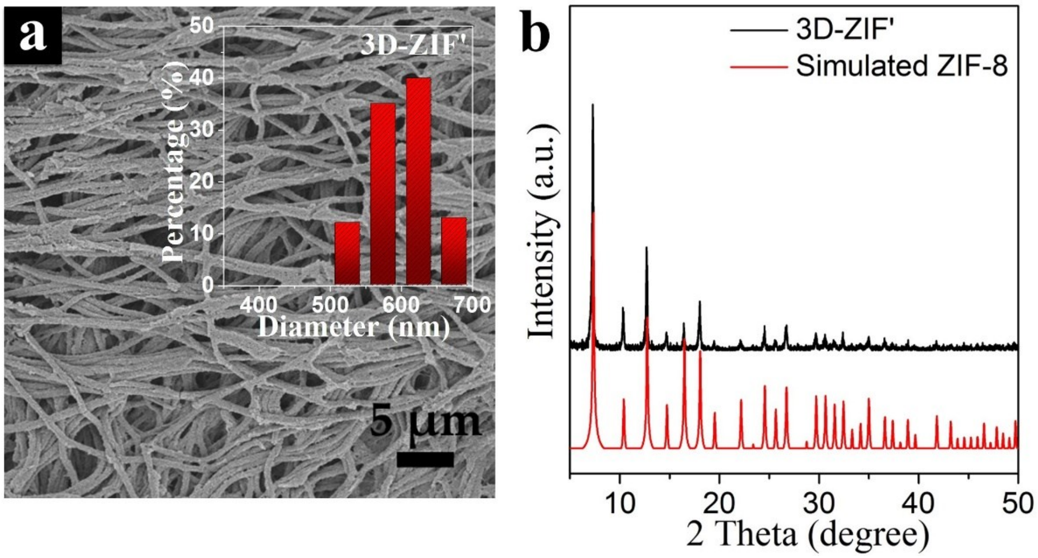

Fig. S5. (a) FESEM image of 3D-ZIF’ tubes. Inset is the diameter distribution of 3D-ZIF’ tubes calculated from the FESEM image; (b) XRD patterns of 3D-ZIF’ tubes and simulated ZIF-8.

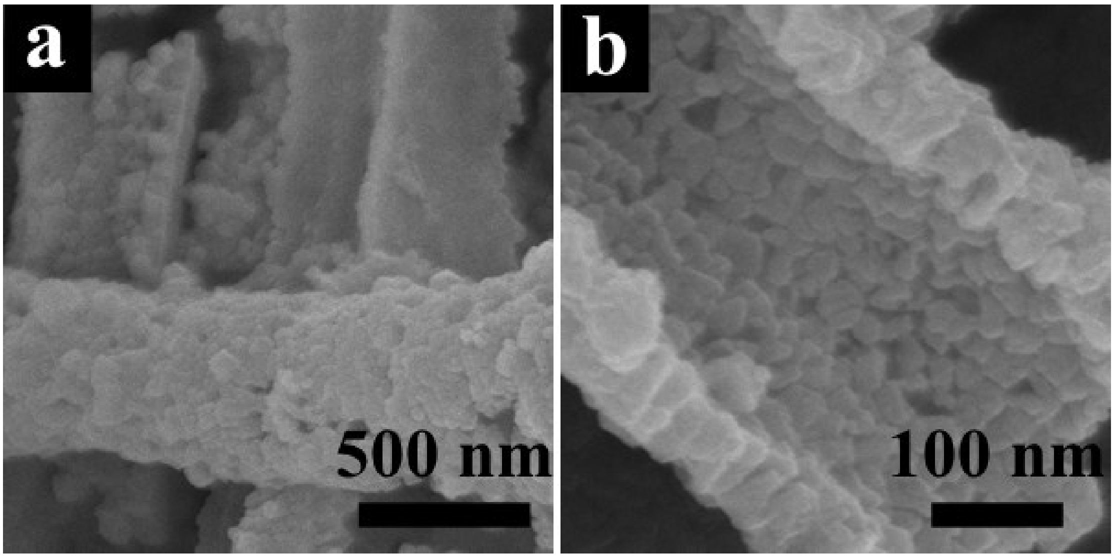

Fig. S6. (a) Low- and (b) high-resolution FESEM images of ZIF’ tubes prepared by using pure PAN as a template.

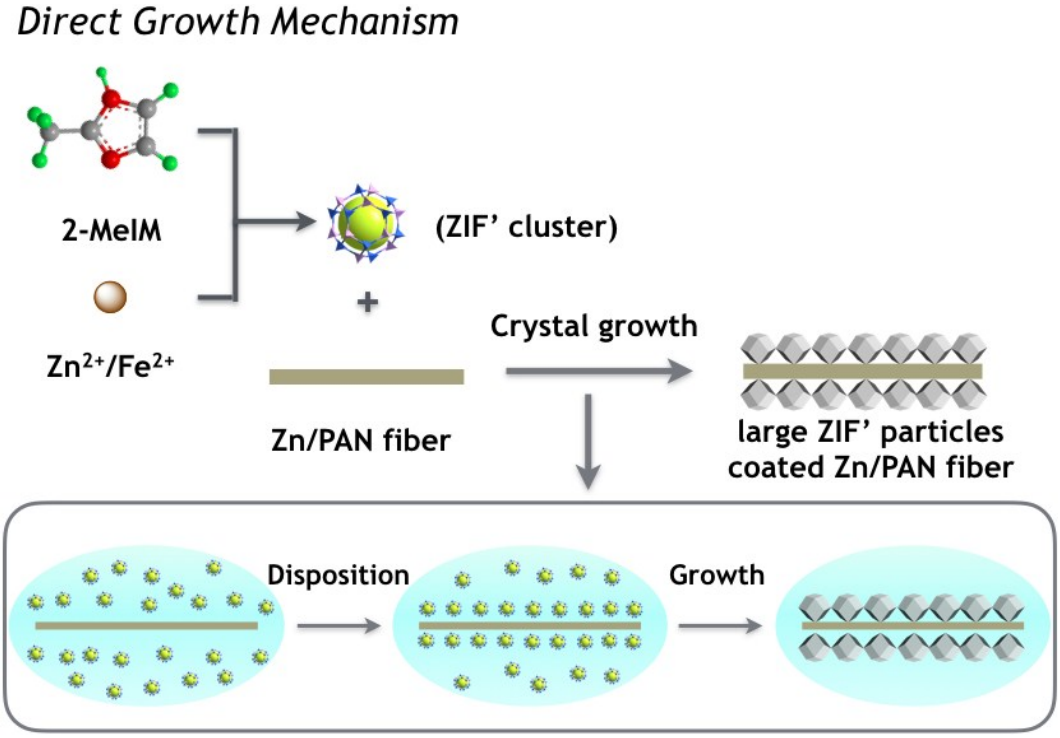

Fig. S7. Schematic diagram depicting the direct immersion of Zn/PAN fibers in a mixed solution containing the metal precursor and the organic ligand. ZIF’ layer composed of large ZIF’ particles is formed.

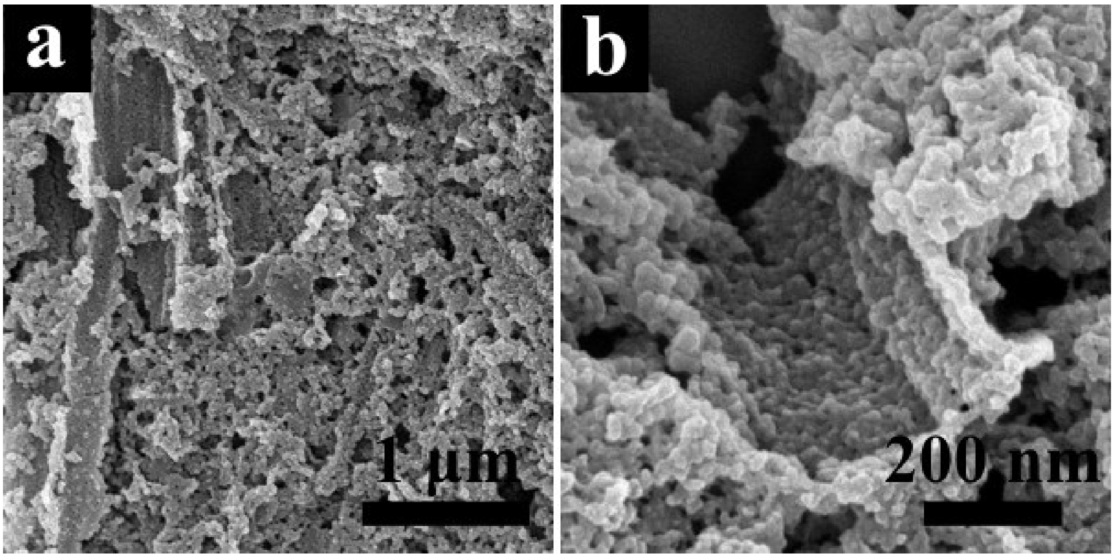

Fig. S8. (a) Low- and (b) high-resolution FESEM images of ZIF' tubes prepared by direct growth method.

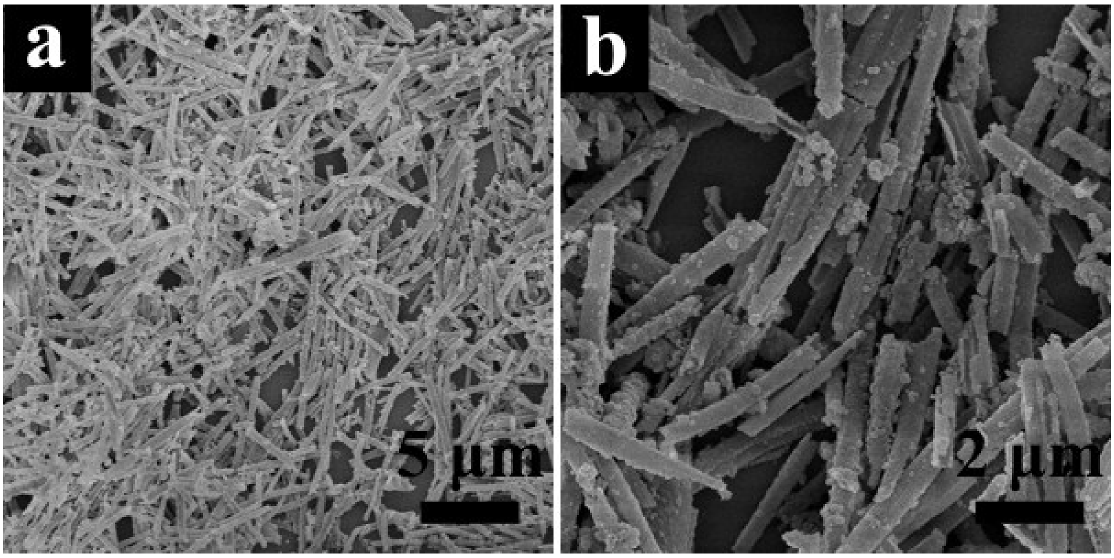

Fig. S9. (a) Low- and (b) high-resolution FESEM images of ZIF' tubes obtained by three times repeated alternate immersion.

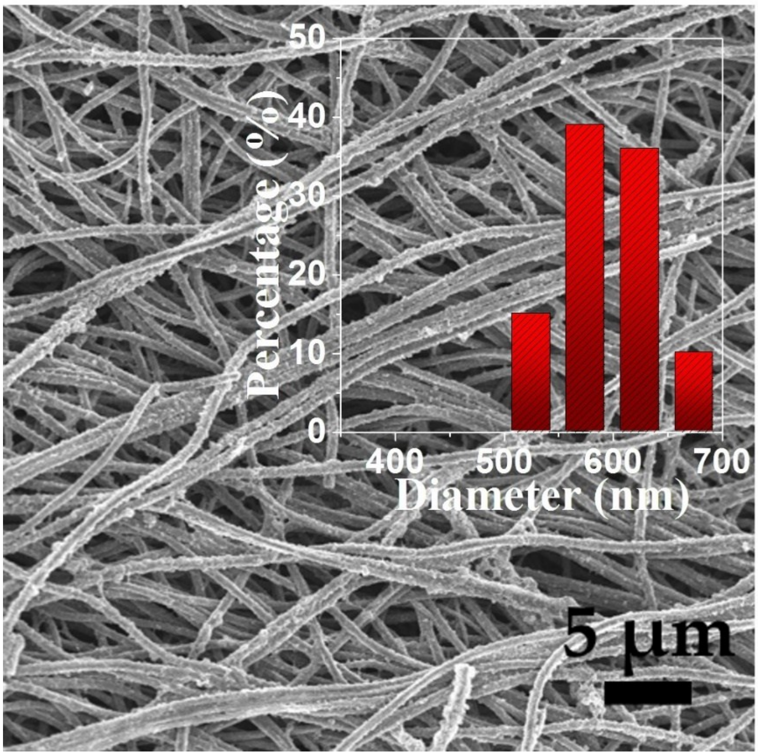

Fig. S10. FESEM image of continuous 3D-FeNC tubes. Inset is the diameter distribution of 3D-FeNC tubes calculated from the FESEM image.

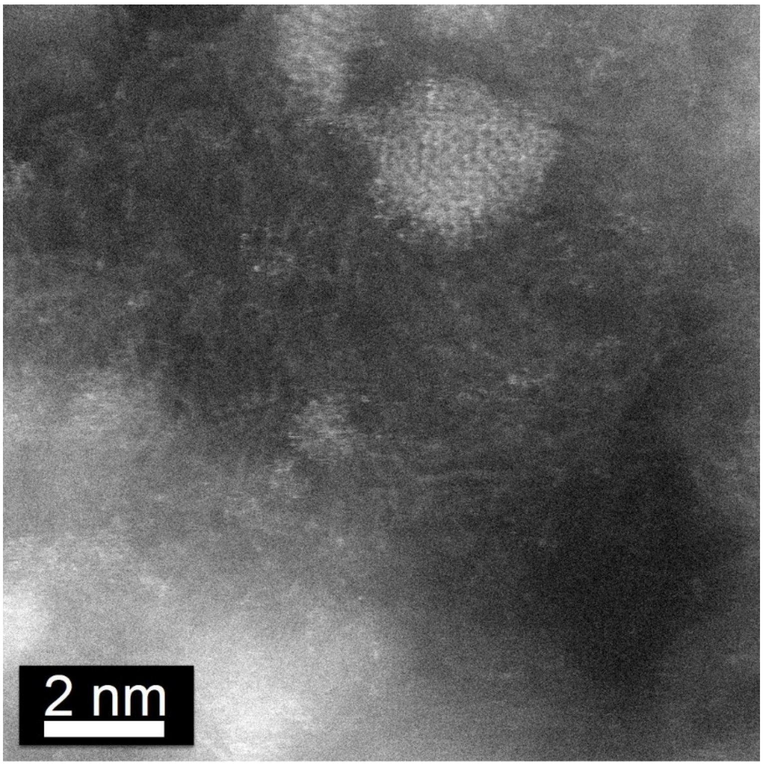

Fig. S11. HAADF-STEM image of 3D-FeNC tubes.

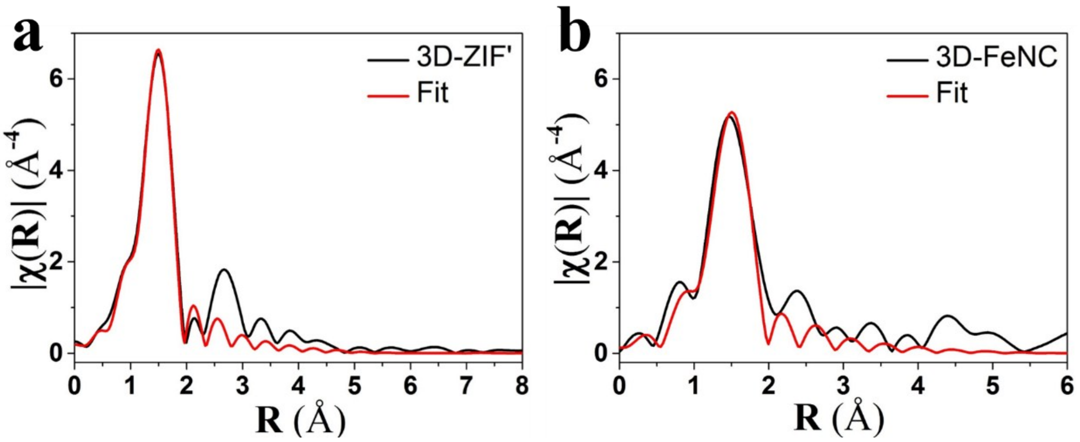

Fig. S12. Fe K-edge EXAFS fitting of (a) 3D-ZIF' and (b) 3D-FeNC tubes.

Supplementary Note 1 for Fig. S12: To further confirm the coordination of Fe to N and to investigate the quantitative chemical configuration of Fe atom, EXAFS fitting was performed on the first shell of 3D-ZIF' and 3D-FeNC (**Fig. S12 and Table S1**). The coordination number of Fe in 3D-ZIF' precursor can be well-fitted with approximately four N atoms. The Fe atoms in 3D-FeNC have a reduced coordination number of about three N atoms and this is in good agreement with the result of X-ray absorption near edge structure (**Fig. 3d**) analysis. According to the above analysis, Fe atoms in 3D-FeNC are atomically anchored in the nitrogen doped carbon frameworks and are coordinated by less than four N atoms. In addition, a few small Fe nanoparticles are also dispersed in 3D-FeNC.

Table S1. Fitting parameters of Fe K-edge EXAFS spectra of 3D-ZIF' and 3D-FeNC.[a]

Sample	Shell	*CN*	*R* (Å)	σ^2 (Å^2)	ΔE_0(eV)	R_f
3D-ZIF'[b]	Fe-N	4(0.43)	1.98(5)	0.007(0)	-5.0(4)	0.002
3D-FeNC[c]	Fe-N	3.01(1.37)	2.00(0)	0.006(2)	-3.1(3)	0.024

[a] *CN*, coordination number; *R*, distance between absorber and backscatter atoms; σ^2, Debye–Waller factor to account for both thermal and structural disorders; ΔE_0, edge-energy shift (the difference between the zero kinetic energy value of the sample and that of the theoretical model). R_f factor is used to assess the quality of the fitting. The single number in the bracket for *R*, σ^2 and ΔE_0 is the last digit error, while the number in the bracket for *CN* is the full error.

[b] Fitting range: $3.0 \leq k$ (Å^{-1}) ≤ 10.4; $1.0 \leq R$ (Å) ≤ 2.1.

[c] Fitting range: $3.0 \leq k$ (Å^{-1}) ≤ 9.9; $1.0 \leq R$ (Å) ≤ 2.1.

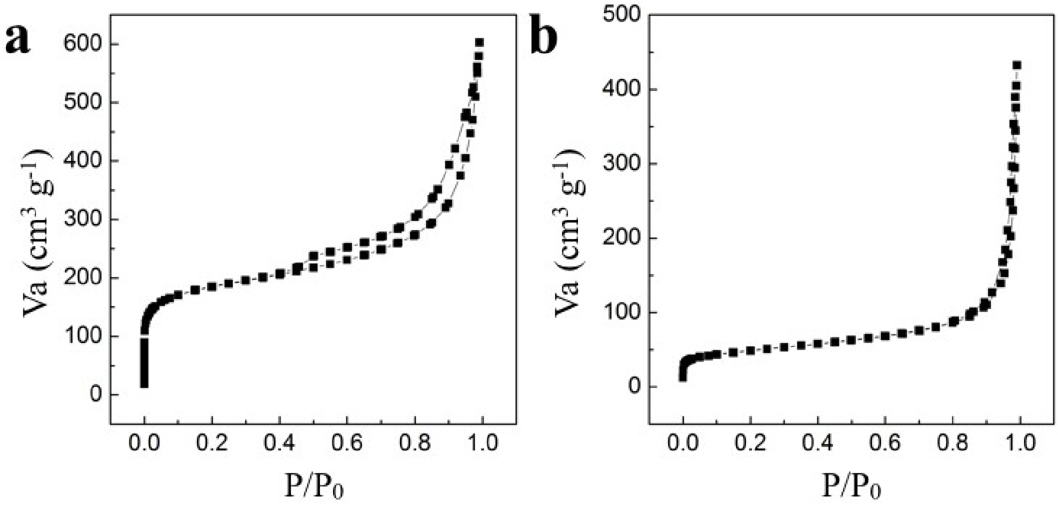

Fig. S13. N_2 adsorption-desorption isotherms of (a) p-FeNC and (b) Pt/C.

Table S2. Comparison of ORR activities of all the investigated materials.

Sample	*SSA* (m^2 g^{-1})	Onset potential (E_{onset}, mV)	Half-wave potential ($E_{1/2}$, mV)	Diffusion-limiting current density (I_L, mA cm^{-2})
3D-FeNC	994.6[a]	0.98	0.877	5.60
p-FeNC	665.9	0.91	0.811	3.67
Pt/C	169.6	1.01	0.848	5.71

[a] The SSA of 3D-FeNC is analyzed in **Fig. S16**.

Supplementary Note 3 for Figs. 5a, b, Fig. S13 and Table S2: CV curves of all the tested materials (Pt/C, p-FeNC, and 3D-FeNC tubes) clearly reveal the presence of oxygen reduction peaks in O_2-saturated 0.1 M KOH solution compared with those in N_2-saturated solution, implying the activity for ORR (**Fig. 5a**). The oxygen reduction peaks of Pt/C, p-FeNC, and 3D-FeNC tubes are observed at 0.84, 0.78, and 0.86 V (*vs.* RHE), respectively. Note that 3D-FeNC tubes show a more positive potential than p-FeNC, suggesting that the novel 3D continuous tubular structure of 3D-FeNC tubes plays an important role in enhancing its ORR activity. The 3D-FeNC tubes combine several advantages, including numerous exposed active sites, larger accessible SSA, shortened electronic-ionic diffusion pathway (resulting from the hollow tube structure1D carbon tube), and continuous electrically-conductive network (arising from the 3D interconnected structure), thereby leading to the enhanced ORR activity. Even compared with commercial Pt/C (0.84 V), the as-prepared 3D-FeNC tubes still exhibit a more positive potential (0.86 V).

LSV curves of all catalysts measured using a RRDE in O_2-saturated 0.1 M KOH solution reveal a similar trend with the CV curves (**Fig. 5b**). It is well known that onset potential (E_{onset}), half-wave potential ($E_{1/2}$), and diffusion-limiting current density (I_L) are important parameters to describe the ORR activity of a particular catalyst. As supported by the LSV curves, the 3D-FeNC catalyst displays a higher half-wave potential ($E_{1/2}$ = 0.877 V *vs.* RHE) and onset potential (E_{onset} = 0.98 V *vs.* RHE) than both p-FeNC ($E_{1/2}$ = 0.811 V; E_{onset} = 0.91 V) and Pt/C ($E_{1/2}$ = 0.848 V; E_{onset} = 1.01 V), implying its superior ORR activity. The diffusion-limiting current densities at 0.60 V are 5.71, 3.67, and 5.60 mA cm^{-2} for Pt/C, p-FeNC, and 3D-FeNC tubes, respectively. The 3D-FeNC catalyst shows a relatively similar diffusion-limiting current density as the commercial Pt/C catalyst, possibly due to its novel 3D continuous tubular structure which may promote faster mass transport and exchange at a more positive potential as well as abundant and highly exposed active sites.

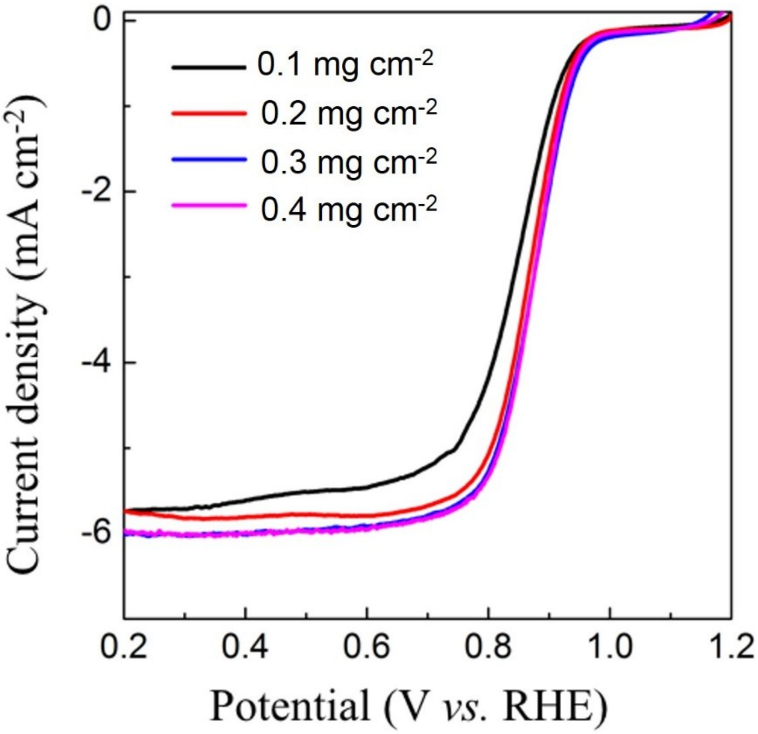

Fig. S14. LSV curves of 3D-FeNC-5 with various mass loading.

Supplementary Note 4 for Fig. S14: The effect of mass loading of the 3D-FeNC-5 catalyst on its ORR activity was investigated (**Fig. S14**). Clearly, when the catalyst loading is below 0.2 mg cm^{-2}, the increase of catalyst loading can largely improve ORR activity in terms of both diffusion-limiting current density and half-wave potential. However, when the mass loading is higher than 0.2 mg cm^{-2}, the ORR activity is barely enhanced with the increase of mass loading.

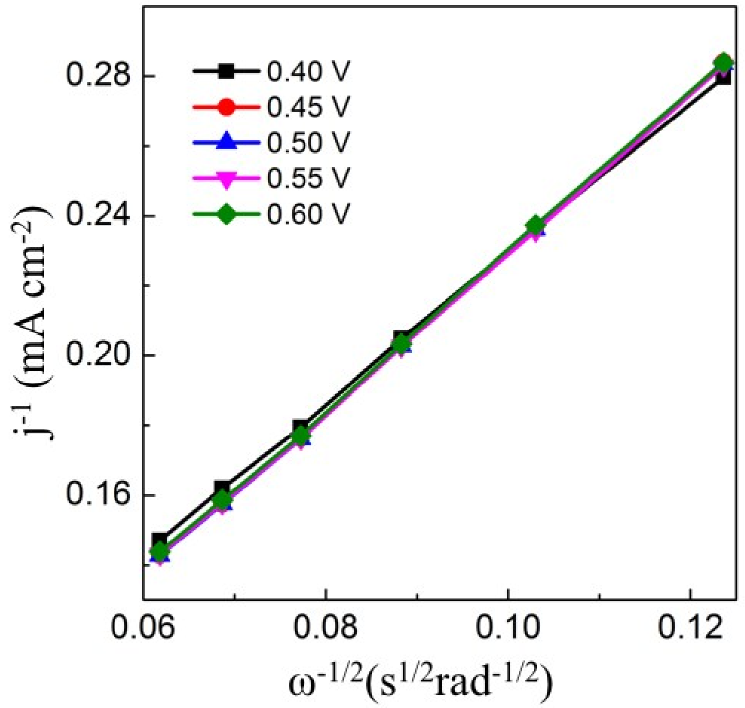

Fig. S15. K-L plots of 3D-FeNC tubes.

Supplementary Note 5 for Figs. 5c and S15: The LSV curves of the 3D-FeNC catalyst at various rotating speed from 625 to 2500 rpm were obtained at a constant potential in O_2-saturated 0.1 M KOH solution (**Fig. 5c**). The K-L plots under different potentials are parallel with good linearity (**Fig. S15**), suggesting first-order reaction kinetics based on the concentration of dissolved oxygen in the ORR setup at different potentials.[2] The number of transferred electrons (n) calculated from K-L plots is 3.92–3.94 between 0.40 and 0.60 V, confirming that the ORR process proceeds *via* a four-electron pathway in 3D-FeNC.

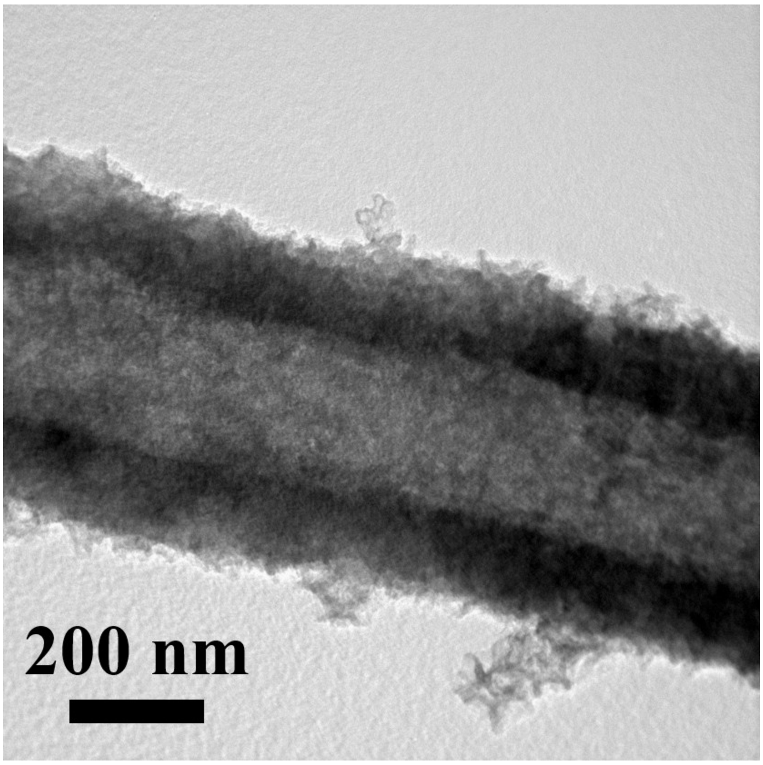

Fig. S16. TEM image of 3D-FeNC after an accelerated degradation test.

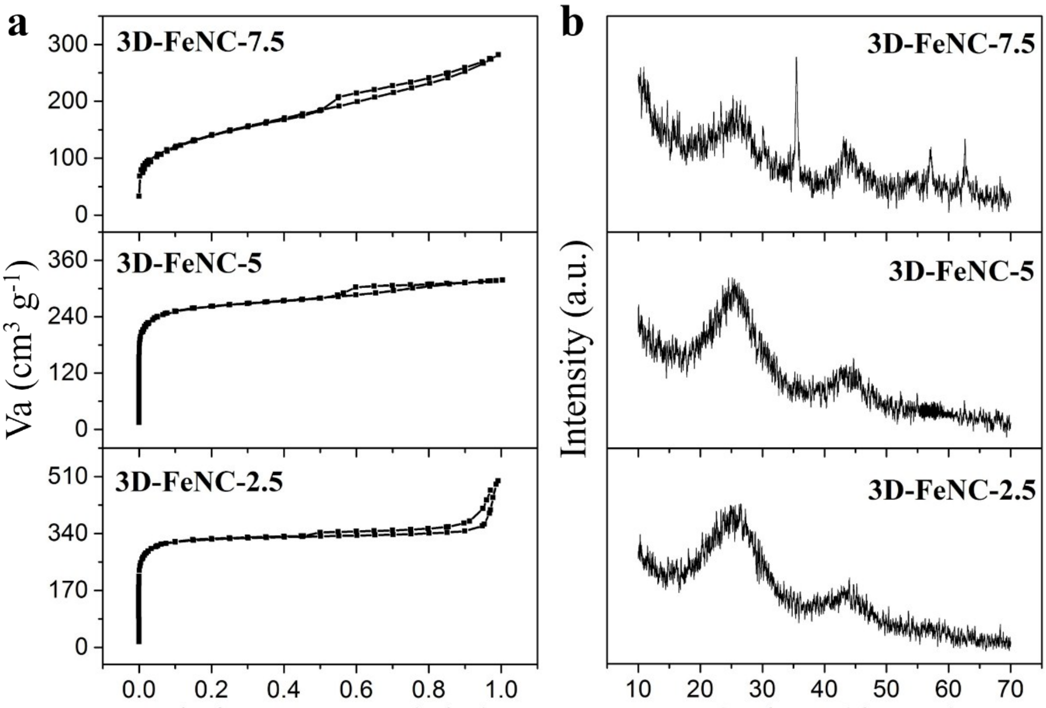

Fig. S17. (a) N_2 adsorption-desorption isotherms and (b) XRD patterns of 3D-FeNC-2.5, 3D-FeNC-5, and 3D-FeNC-7.5.

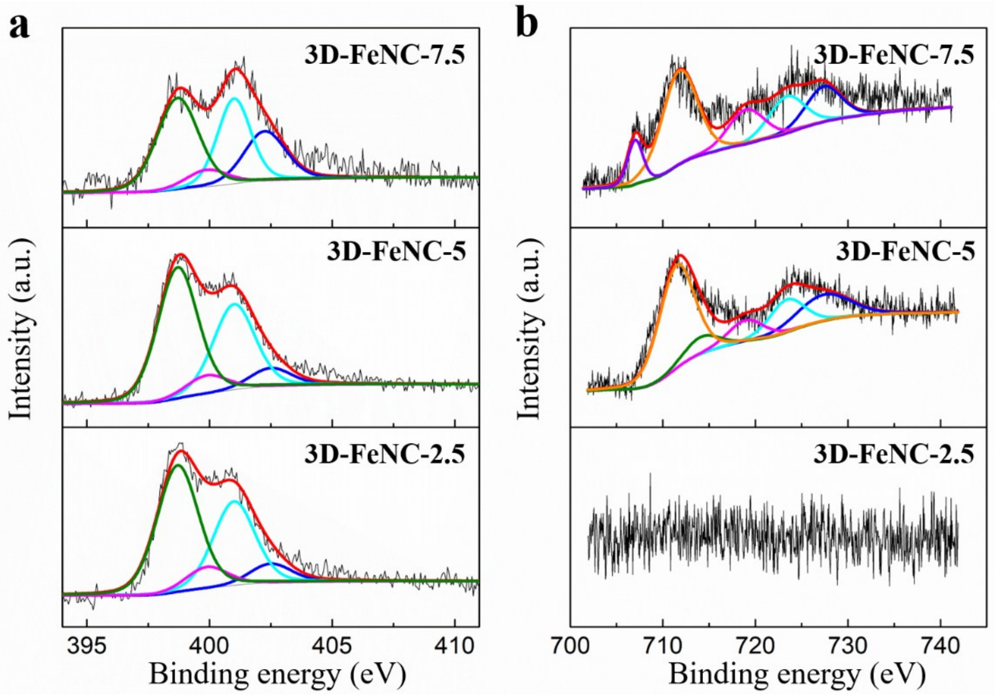

Fig. S18. High-resolution XPS spectra of (a) N 1*s* and (b) Fe 2*p* for 3D-FeNC-2.5, 3D-FeNC-5, and 3D-FeNC-7.5.

Table S3. Structural parameters of 3D-FeNC-2.5, 3D-FeNC-5, and 3D-FeNC-7.5. The N content was estimated from the N 1*s* XPS spectra and the exact content of Fe was estimated by ICP-OES.

Sample	SSA (m^2g^{-1})	N (at.%)	Fe (wt.%)
3D-FeNC-2.5	1239.7	12.1	0.6
.3D-FeNC-5	994.6	10.5	1.4
3D-FeNC-7.5	495.2	4.6	2.3

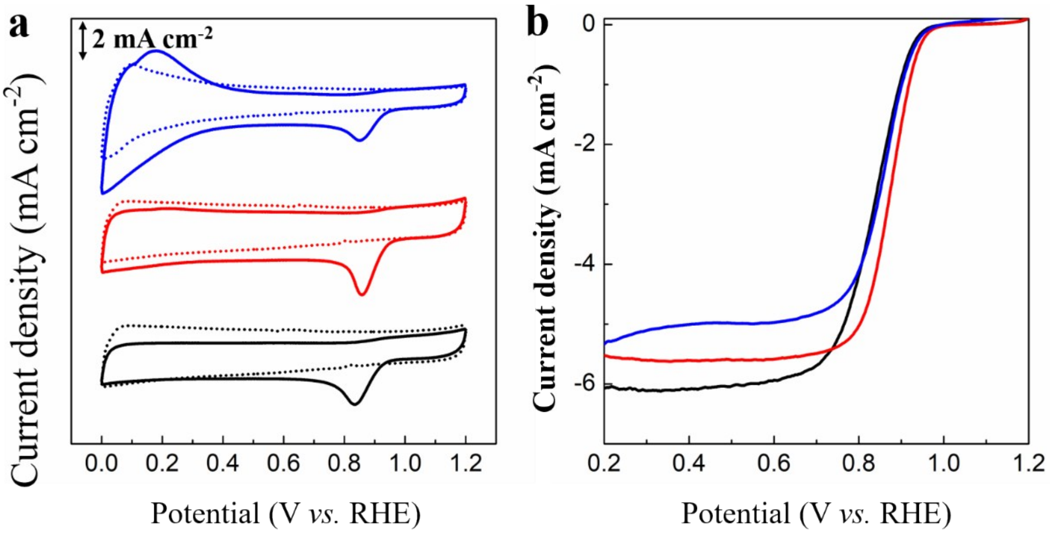

Fig. S19. (a) CV and (b) LSV curves of 3D-FeNC-2.5 (Black), 3D-FeNC-5 (Red), and 3D-FeNC-7.5 (Blue) catalysts in N_2 (dot line)/O_2 (solid line)-saturated 0.1 M KOH solution.

Table S4. Comparison of the ORR activity of 3D-FeNC-*y* (*y*=2.5, 5, and 7.5) and other iron-nitrogen co-doped carbon materials.

Sample	Onset potential (E_{onset}, V)	Half-wave potential ($E_{1/2}$, V)	Diffusion-limiting current density (I_L, mA cm^{-2})	Mass loading (*m*, μg cm^{-2})	Gravimetric current density (I_g, mA μg^{-1})[a]	Ref.
3D-FeNC-2.5	0.95	0.837	5.98	1.2	4.98	This work
3D-FeNC-5	0.98	0.877	5.60	2.4	2.33	
3D-FeNC-7.5	0.96	0.858	4.98	4.6	1.08	
NH_3-Fe0.25-N/C-900	1.018	0.865	5.98	0.5	11.96	3
Fe1.6-N-HCNS/rGO-900	–	0.872	5.68	1.6	3.55	4
Fe-N-GC-900 (2:1)	0.88	0.74	5.3	–	–	5
Fe-NMCSs	1.027	0.86	*ca.* 5.2	~2.7	1.93	6
Fe-NG	0.965	0.826	7.2	~14.8	0.49	7
Fe−N−CC	0.94	ca. 0.83	ca. 4.3	0.7	6.14	8
Fe-N-C/KB	0.92	0.78	5.7	–	–	9
pCNT@Fe1.5@GL	0.957 ± 0.007 (the potential at 0.3 mA cm^{-2})	0.867 ± 0.005	5.5–6.0	3	1.83–2	10

[a] The gravimetric current density (I_g, mA μg^{-1}) was used to indicate the specific ORR activity, and was calculated as follows: $I_g=I/m$. *I* is the diffusion-limiting current density (mA cm^{-2}) of LSV curve and *m* is the mass loading of the catalyst (μg cm^{-2}).

Supplementary Note 8 for Fig. S19 and Table S4: 3D-FeNC-*y* (*y*=2.5, 5, and 7.5) catalysts have obvious oxygen reduction peaks in O_2-saturated 0.1 M KOH solution compared to those in N_2-saturated solution, implying the activity. The 3D-FeNC-5 catalyst shows a more positive oxygen reduction peak than both 3D-FeNC-2.5 and 3D-FeNC-7.5 catalysts (**Fig. S19a**). LSV curves of the catalysts show a similar trend as the CV curves. With the increase of Fe content in 3D-FeNC tubes, the half-wave potential and onset potential increase from $E_{1/2}$ = 0.837 V *vs.* RHE and E_{onset} = 0.95 V *vs.* RHE for 3D-FeNC-2.5 to $E_{1/2}$ = 0.877 V *vs.* RHE and E_{onset} = 0.98 V *vs.* RHE for 3D-FeNC-5, then decrease to $E_{1/2}$ = 0.858 V *vs.* RHE and E_{onset} = 0.96 V *vs.* RHE for 3D-FeNC-7.5. However, the diffusion-limiting current density decreases with the increase of Fe content in 3D-FeNC tubes. Combining these points, the 3D-FeNC-5 catalyst exhibits the highest ORR activity among the 3D-FeNC-*y* (*y*=2.5, 5, and 7.5) materials (**Fig. S19b** and **Table S4**). This may be attributed to the higher content of Fe in 3D-ZIF' precursor, which leads to easier aggregation of Fe and increased graphitization degree during the carbonization process, thereby leading to decreased SSA, reduced nitrogen content, and less effective Fe-based ORR active sites (**Figs. S17** and **S18**).

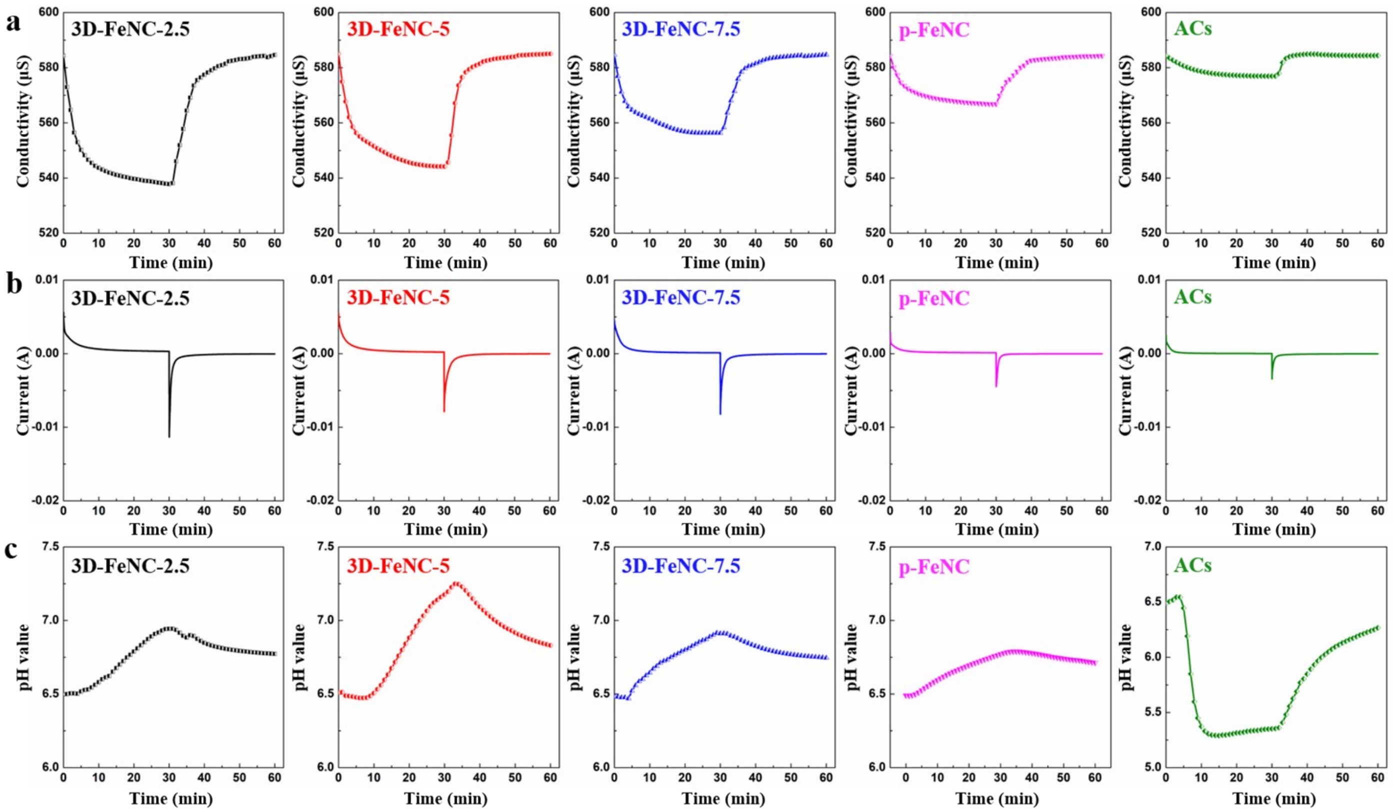

Fig. S20 Full-cycle (a) conductivity, (b) current, and (c) pH value profiles of 3D-FeNC-*y* (*y* = 2.5, 5 and 7.5), p-FeNC, and commercial AC in oxygenated saline water (5 mM).

Supplementary Note 9 for Fig. S20: The full-cycle conductivity profiles shown in **Fig. S20a** indicate that all materials possess good desalination/regeneration ability. Combined with the synchronously-recorded current profiles (**Fig. S20b**), the charge efficiencies of all materials are calculated to be around 0.58~0.59, and specific energy consumptions are in the range of 3.3~3.4 J mg^{-1}, which are slightly different from other reports, mainly due to the enhanced ORR in oxygenated saline water. The pH value profiles (**Fig. S20c**) reveal that 3D-FeNC and p-FeNC exhibit higher activities for ORR than commercial AC with increasing pH, possibly due to the accelerated consumption of H^{+} through the enhanced ORR. Moreover, the higher ORR activity may also lead to a greater change in pH value.

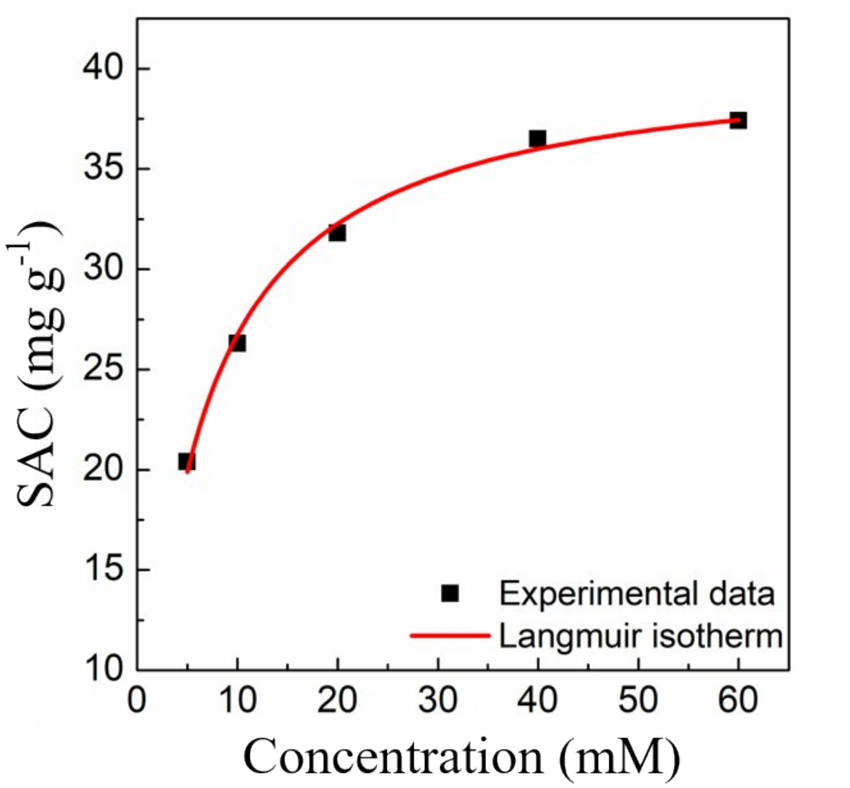

Fig. S21. Langmuir isotherm together with experimental data of 3D-FeNC-5 in oxygenated saline water.

Table S5. Coefficients of Langmuir fitting.

Isotherm	Model equation	Parameter	Value
Langmuir	$q = \frac{q_m K_L C}{1 + K_L C}$	q_m	40.70
		K_L	0.191
		r^2	0.994

Supplementary Note 8 for Fig. S21 and Table S5: The purpose of the electrosorption isotherm is to relate the NaCl concentration in the bulk solution and the SAC at the interface. The analysis of the isotherm data is important to develop an equation which accurately represents the results and can be used for designing purpose. It is well known that Langmuir and modified Donnan models are two common tools to analyze the maximum SAC of carbon materials. In particular, the modified Donnan model which has been developed by Biesheuvel *et al*[11] is very useful to fully interpret the double-layer structure inside the electrode. However, considering complicated nature of electrochemical processes in this work, which involve both electrosorption and four-electron ORR reaction, we have chosen not to use the modified Donnan model in this study. Instead, the Langmuir isotherm model was utilized to simply simulate the experimental data for CDI process of 3D-FeNC-5 electrode in oxygenated saline water as described by the following equation:

$$q = \frac{q_m K_L C}{1 + K_L C} \tag{S7}$$

where q is the SAC (mg g^{-1}), q_m is the maximum SAC (mg g^{-1}) corresponding to complete monolayer coverage, C is the equilibrium concentration (mM), and K_L is the Langmuir constant related to the free energy of electrosorption. The simulated and experimental data are presented in **Fig. S21** and **Table S5**, respectively. It is found that the maximum SAC (q_m) predicted from the isotherm is 40.70 mg g^{-1}, which is much higher than those of previously reported carbon materials (**Table S6**), demonstrating the superiority of 3D-FeNC-5 for CDI application.

Table S6. Performance comparison of 3D-FeNC-5 and other carbon materials.

Sample	SSA ($m^2\ g^{-1}$)	Voltage (V)	SAC ($mg\ g^{-1}$)	Ref.
P-60	1260	1.5	5.28	12
Filtrasorb 400	964	1.0	13.03	13
AC-1-2.0	2105	1.0	9.72	14
C5A85K4	3649	1.2	22.2	15
HPC	609	1.2	10.27	16
CCS	2680	1.2	16.1	17
3DHCA	2061	1.2	17.83	18
PCNSs	2853	1.1	15.6	19
NPC	1036.2	1.2	15.5	20
SBB-CO2-30	1019	1.2	28.9	21
CTS-AC	2727	1.2	14.12	22
PCS1000	1321	1.6	5.81	23
NPCSs1000	1640	1.2	14.91	24
N-PHCS	512	1.4	12.95	25
hCSs-800	1529	1.2	15.8	26
PCSs-800	485.6	1.2	18.5	27
CHS-1	809.91	1.6	18.88	28
N-HMCSs	1099	1.6	16.6	29
OMC	844	1.2	0.68	30
NMCs	842.3	1.2	20.63	31
NOMC	459.32	1.6	26.2	32
OMC-O	1481	1.2	9.8	33
o-OMCs-1000	780.3	1.2	14.58	34
OMC-S	1491	1.2	0.93	35
ACk2	1968	1.6	11.7	36
N-HMCS/HGH	337.7	1.4	37.2	37
GSSNA-11	664	1.2	22.09	38
CSG	711.9	1.5	9.60	39

GE/MC	685.2	2.0	0.73	40
MC	1700	1.2	3.5	41
Activated graphene	3513	2.0	11.86	42
G@MC-O-thin	1270	1.2	24.3	43
AGE-30	898	1.2	6.26	44
RGO/AC	779	1.2	2.94	45
GTAC	426.56	1.2	10.94	46
GS	356.0	1.2	14.9	47
mGE	474.0	1.2	14.2	48
HGF	124	2.0	29.6	49
EPD-CNTs	82	1.2	2.33	50
CNTs/CNFs	211	1.2	1.61	51
MWCNT/PVA	208	1.2	13.07	52
nit-CNTs	200.9	1.2	17.18	53
ZFCarbon	2060	1.2	8.1	54
e-CNF-PCP	1450.6	1.2	12.56	55
PC-900	1563.09	1.2	9.39	56
PC-900	1911	1.2	10.90	57
NC-800	798	1.2	8.52	58
PCP1200	1187.8	1.2	13.86	59
ZIF-8@PZS-C	929	1.2	22.19	60
A-NCP	2474	1.2	24.4	61
aG10P	1067	1.2	36.1	62
3D-FeNC-5	**994.6**	**1.2**	**40.70**	**This work**

Supplementary References

1. M. Sokół, J. Grobelny and E. Turska, *Polymer*, 1987, **28**, 843-846.
2. X. Fan, Y. Liu, Z. Peng, Z. Zhang, H. Zhou, X. Zhang, B. I. Yakobson, W. A. Goddard III, X. Guo and R. H. Hauge, *ACS Nano*, 2017, **11**, 384-394.
3. H. Tan, Y. Li, X. Jiang, J. Tang, Z. Wang, H. Qian, P. Mei, V. Malgras, Y. Bando and Y. Yamauchi, *Nano Energy*, 2017, **36**, 286-294.
4. H. Tan, J. Tang, J. Henzie, Y. Li, X. Xu, T. Chen, Z. Wang, J. Wang, Y. Ide, Y. Bando and Y. Yamauchi, *ACS Nano*, 2018, **12**, 5674-5683.
5. A. Kong, X. Zhu, Z. Han, Y. Yu, Y. Zhang, B. Dong and Y. Shan, *ACS Catal.*, 2014, **4**, 1793-1800.
6. F.-L. Meng, Z.-L. Wang, H.-X. Zhong, J. Wang, J.-M. Yan and X.-B. Zhang, *Adv. Mater.*, 2016, **28**, 7948-7955.
7. X. Cui, S. Yang, X. Yan, J. Leng, S. Shuang, P. M. Ajayan and Z. Zhang, *Adv. Funct. Mater.*, 2016, **26**, 5708-5717.
8. G. A. Ferrero, K. Preuss, A. Marinovic, A. B. Jorge, N. Mansor, D. J. L. Brett, A. B. Fuertes, M. Sevilla and M.-M. Titirici, *ACS Nano*, 2016, **10**, 5922-5932.
9. S. Bukola, B. Merzougui, A. Akinpelu, T. Laoui, M. N. Hedhili, G. M. Swain and M. Shao, *Electrochim. Acta*, 2014, **146**, 809-818.
10. S. H. Ahn, X. Yu and A. Manthiram, *Adv. Mater.*, 2017, **29**, 1606534.
11. P. Biesheuvel, S. Porada, M. Levi and M. Z. Bazant, *J. Solid State Electrochem.*, 2014, **18**, 1365-1376.
12. Y.-J. Kim and J.-H. Choi, *Sep. Purif. Technol.*, 2010, **71**, 70-75.
13. C.-H. Hou and C.-Y. Huang, *Desalination*, 2013, **314**, 124-129.
14. C.-L. Yeh, H.-C. Hsi, K.-C. Li and C.-H. Hou, *Desalination*, 2015, **367**, 60-68.
15. R. L. Zornitta, K. M. Barcelos, F. G. E. Nogueira and L. A. M. Ruotolo, *Carbon*, 2020, **156**, 346-358.
16. Y. Li, I. Hussain, J. Qi, C. Liu, J. Li, J. Shen, X. Sun, W. Han and L. Wang, *Sep. Purif. Technol.*, 2016, **165**, 190-198.
17. G.-X. Li, P.-X. Hou, S.-Y. Zhao, C. Liu and H.-M. Cheng, *Carbon*, 2016, **101**, 1-8.
18. S. Zhao, T. Yan, H. Wang, J. Zhang, L. Shi and D. Zhang, *ACS Appl. Mater. Interfaces*, 2016, **8**, 18027-18035.
19. T. Wu, G. Wang, Q. Dong, F. Zhan, X. Zhang, S. Li, H. Qiao and J. Qiu, *Environ. Sci. Technol.*, 2017, **51**, 9244-9251.
20. C. Zhao, G. Liu, N. Sun, X. Zhang, G. Wang, Y. Zhang, H. Zhang and H. Zhao, *Chem. Eng. J.*, 2018, **334**, 1270-1280.
21. Y.-H. Tang, S.-H. Liu and D. C. W. Tsang, *J. Hazard. Mater.*, 2020, **383**, 121192.
22. Q. Wu, D. Liang, X. Ma, S. Lu and Y. Xiang, *RSC Adv.*, 2019, **9**, 26676-26684.
23. Y. Liu, L. Pan, T. Chen, X. Xu, T. Lu, Z. Sun and D. H. C. Chua, *Electrochim. Acta*, 2015, **151**, 489-496.

24. Y. Liu, T. Chen, T. Lu, Z. Sun, D. H. C. Chua and L. Pan, *Electrochim. Acta*, 2015, **158**, 403-409.
25. S. Zhao, T. Yan, H. Wang, G. Chen, L. Huang, J. Zhang, L. Shi and D. Zhang, *Appl. Surf. Sci.*, 2016, **369**, 460-469.
26. X. Xu, H. Tang, M. Wang, Y. Liu, Y. Li, T. Lu and L. Pan, *J. Mater. Chem. A*, 2016, **4**, 16094-16100.
27. Y. Li, X. Xu, S. Hou, J. Ma, T. Lu, J. Wang, Y. Yao and L. Pan, *Chem. Commun.*, 2018, **54**, 14009-14012.
28. Z. Y. Leong and H. Y. Yang, *RSC Adv.*, 2016, **6**, 53542-53549.
29. Y. Li, J. Qi, J. Li, J. Shen, Y. Liu, X. Sun, J. Shen, W. Han and L. Wang, *ACS Sustain. Chem. Eng.*, 2017, **5**, 6635-6644.
30. L. Zou, L. Li, H. Song and G. Morris, *Water Res.*, 2008, **42**, 2340-2348.
31. X. Xu, A. Enaiet Allah, C. Wang, H. Tan, A. A. Farghali, M. Hamdy Khedr, V. Malgras, T. Yang and Y. Yamauchi, *Chem. Eng. J.*, 2019, **362**, 887-896.
32. S. Tian, J. Wu, X. Zhang, K. Ostrikov and Z. Zhang, *Chem. Eng. J.*, 2020, **380**, 122514.
33. F. Duan, X. Du, Y. Li, H. Cao and Y. Zhang, *Desalination*, 2015, **376**, 17-24.
34. X. Xu, H. Tan, Z. Wang, C. Wang, L. Pan, Y. V. Kaneti, T. Yang and Y. Yamauchi, *Environ. Sci. Nano*, 2019, **6**, 981-989.
35. L. Li, L. Zou, H. Song and G. Morris, *Carbon*, 2009, **47**, 775-781.
36. G. Wang, B. Qian, Q. Dong, J. Yang, Z. Zhao and J. Qiu, *Sep. Purif. Technol.*, 2013, **103**, 216-221.
37. M. Mi, X. Liu, W. Kong, Y. Ge, W. Dang and J. Hu, *Desalination*, 2019, **464**, 18-24.
38. Z. U. Khan, T. Yan, L. Shi and D. Zhang, *Environ. Sci. Nano*, 2018, **5**, 980-991.
39. L. Chang and Y. Hang Hu, *J. Colloid Interface Sci.*, 2019, **538**, 420-425.
40. D. Zhang, X. Wen, L. Shi, T. Yan and J. Zhang, *Nanoscale*, 2012, **4**, 5440-5446.
41. C. Tsouris, R. Mayes, J. Kiggans, K. Sharma, S. Yiacoumi, D. DePaoli and S. Dai, *Environ. Sci. Technol.*, 2011, **45**, 10243-10249.
42. Z. Li, B. Song, Z. Wu, Z. Lin, Y. Yao, K.-S. Moon and C. P. Wong, *Nano Energy*, 2015, **11**, 711-718.
43. O. Noonan, Y. Liu, X. Huang and C. Yu, *J. Mater. Chem. A*, 2018, **6**, 14272-14280.
44. Y. Zhang, L. Chen, S. Mao, Z. Sun, Y. Song and R. Zhao, *J. Colloid Interface Sci.*, 2019, **536**, 252-260.
45. H. Li, L. Pan, C. Nie, Y. Liu and Z. Sun, *J. Mater. Chem.*, 2012, **22**, 15556-15561.
46. G. Zhu, W. Wang, X. Li, J. Zhu, H. Wang and L. Zhang, *RSC Adv.*, 2016, **6**, 5817-5823.
47. X. Xu, L. Pan, Y. Liu, T. Lu, Z. Sun and D. H. C. Chua, *Sci. Rep.*, 2015, **5**, 8458.
48. X. Xu, Y. Liu, M. Wang, X. Yang, C. Zhu, T. Lu, R. Zhao and L. Pan, *Electrochim. Acta*, 2016, **188**, 406-413.
49. J. Li, B. Ji, R. Jiang, P. Zhang, N. Chen, G. Zhang and L. Qu, *Carbon*, 2018, **129**, 95-103.
50. C. Nie, L. Pan, H. Li, T. Chen, T. Lu and Z. Sun, *J. Electroanal. Chem.*, 2012, **666**, 85-88.
51. H. Li, L. Pan, Y. Zhang, L. Zou, C. Sun, Y. Zhan and Z. Sun, *Chem. Phys. Lett.*, 2010, **485**, 161-166.
52. C.-H. Hou, N.-L. Liu, H.-L. Hsu and W. Den, *Sep. Purif. Technol.*, 2014, **130**, 7-14.

53. P. Shi, C. Wang, J. Sun, P. Lin, X. Xu and T. Yang, *Sep. Purif. Technol.*, 2020, **235**, 116196.
54. M. Wang, X. Xu, Y. Liu, Y. Li, T. Lu and L. Pan, *Carbon*, 2016, **108**, 433-439.
55. Y. Liu, J. Ma, T. Lu and L. Pan, *Sci. Rep.*, 2016, **6**, 32784.
56. L. Chang, J. Li, X. Duan and W. Liu, *Electrochim. Acta*, 2015, **176**, 956-964.
57. X. Duan, W. Liu and L. Chang, *J. Taiwan Inst. Chem. Eng.*, 2016, **62**, 132-139.
58. N.-L. Liu, S. Dutta, R. R. Salunkhe, T. Ahamad, S. M. Alshehri, Y. Yamauchi, C.-H. Hou and K. C. W. Wu, *Sci. Rep.*, 2016, **6**, 28847.
59. Y. Liu, X. Xu, M. Wang, T. Lu, Z. Sun and L. Pan, *Chem. Commun.*, 2015, **51**, 12020-12023.
60. J. Zhang, J. Fang, J. Han, T. Yan, L. Shi and D. Zhang, *J. Mater. Chem. A*, 2018, **6**, 15245-15252.
61. J. Kim, J. Kim, J. H. Kim and H. S. Park, *Chem. Eng. J.*, 2019, **382**,122996.
62. Z. Y. Leong, G. Lu and H. Y. Yang, *Desalination*, 2019, **451**, 172-181.